Properties of ITO thin films rapid thermally annealed in different exposures of nitrogen gas

E. R. Ollotu[1, *]. J. S. Nyarige[3]. N. R. Mlyuka[2]. M. E. Samiji[2]. M. Diale[3]

[1]   Physics Department, Mkwawa University College of Education, P.O. Box 2513, Iringa, Tanzania

[2]   Physics Departments, the University of Dar as Salaam, P.O. Box 35063, Dar as Salaam, Tanzania

[3]   Department of Physics, University of Pretoria, Private Bag X20, Hatfield, 0028, South Africa

Address correspondence to E. R. Ollotu. E-mail: manyoolo@gmail.com

Abstract

Indium Tin Oxide (ITO) thin films were Rapid Thermal Annealed (RTA) for 5 minutes at a temperature of 550 ºC in different exposures of nitrogen gas. Effects of these exposures on the structural, morphological, electrical and optical properties of these films were investigated using X-Ray Diffraction (XRD), Atomic Force Microscopy (AFM) and Field Emission-Scanning Electron Microscopy (FE-SEM), Four-point probe and Hall Effect Measurements, and Ultraviolet-Visible-Near Infrared (UV-VIS-NIR) spectrophotometer, respectively. The un-exposed RTA ITO films maintained (400) plane preferential orientation similar to the un-annealed sample. However, this plane preferential orientation was reduced relative to (222) plane for exposed RTA sample. The grains and surface roughness parameters were reduced for exposed and enhanced for un-exposed RTA samples as compared to the un-annealed sample. Relatively higher electrical conductivity, average solar transmittance and bandgap values were observed for ITO films annealed while exposed to nitrogen gas. The exposed RTA ITO films showed sheet resistance of $7.91\,\Omega/\mathrm{sq}$, average solar transmittance of 83 % and bandgap of 3.93 eV. Findings from this study suggest that RTA exposure have the potential to control ITO thin films properties, hence, extending its potential applications.

Keywords: Indium tin oxide, RTA exposures, structure, optical, electrical

1   Introduction

Demands for energy materials that are readily available, low cost and easy to process have led to the development of novel optoelectronics and solar cells materials [1–6]. Application of such materials on the commonly used electrodes for optoelectronic devices needs further research to achieve such devices best performance. Indium Tin Oxide (ITO) thin films being a transparent conductor with outstanding optical and electrical properties, has been extensively studied as transparent electrodes for organic light-emitting devices, liquid crystal displays, and solar cells [7]. Its high bandgap (above 3.7 eV) and n-type degenerate doping make ITO highly transmit visible radiation and conduct electric current, respectively. This conductivity in ITO thin films emanates from charge carriers donated by Sn^{+4} doping into In_2O_3 lattice and doubly charged oxygen vacancies [8]. Besides, vacancy-like oxygen defects are reported to contribute charge carriers where Sn is considered inefficiently activated [7,9]. Post-deposition annealing in different annealing atmosphere is carried out in such ITO films to efficiently activate Sn. This annealing also improves the film's surface morphology, optical, and electrical properties [10].

Post-deposition annealing experiments are also conducted on ITO thin films to examine these films ability to withstand typical conditions subjected to it when making a device [11]. Such experiments, for example, is preferred on ITO thin films intended for bifacial copper-zinc-tin-sulphide/selenide (CZTS) or copper-indium-gallium-sulphide/selenide (CIGS) solar cells back electrical contact. In these solar cells design, the absorber deposited on a transparent electrode such as ITO thin films is annealed at temperatures above 500 ºC while exposed or unexposed to the annealing ambient as a typical condition to crystalize the absorber [12,13]. Such annealing conditions are likely to differently affect the ITO thin film back contacts properties. In this regard, the post-deposition annealing experiment is desired in such conditions to examine ITO thin films potential to preserve its properties for such applications.

In this work, ITO thin films coated on a glass substrate were RTA at 550 ºC for 5 minutes; one film exposed while another un-exposed to nitrogen gas. The effects of these conditions on the structure, morphological, optical and electrical properties of ITO thin films were investigated using XRD, AFM and FE-SEM, Four-point probe and Hall Effect Measurements, and UV-VIS-NIR spectrophotometer, respectively. Results from this study reveal that these annealing conditions influence ITO films properties.

2 Experiment

2.1 Sample preparation

Commercial ITO coated glass $(3\text{cm} \times 2\text{cm} \times 1 \text{ mm})$ was ultrasonically cleaned in a Decon FS300 frequency sweeper for 25 minutes in distilled water, rinsed and dried in ethanol vapour. Cleaned ITO glass was placed in a graphite box $(6.3\text{cm} \times 3.3\text{cm} \times 2.5\text{cm})$ with the conducting side facing upward and both inserted into the Rapid Thermal Processing (RTP) equipment (RTP 1000D4 furnace) quartz tube. The tube was evacuated using a rotary oil-sealed mechanical pump for 30 minutes, thereafter, nitrogen gas was allowed into the tube at 60 ml/min flow rate. The equipment was then rapidly ramped at 20 ºCsec^{-1} from room temperature to 550 ºC and then remained at this temperature for 5 minutes before naturally cooling down to room temperature. This procedure was simultaneously carried out on un-covered graphite box containing the sample so that the samples were exposed to nitrogen gas and in a covered graphite box so that the samples are not exposed to nitrogen gas. The exposed and un-exposed RTA samples were then characterized and the results compared to the un-annealed samples.

2.2 Sample characterization

The structural properties of the films were analysed using Brucker D2-Phaser X-ray Diffractometer (XRD) using Cu K-alpha radiation with 0.15405 nm wavelength. The 2θ angle was varied from 20° to 85° in steps of 0.05^{o}. The surface roughness parameters and morphology of the films were determined by Veeco Instrument, Nanoscope IIIA Atomic Force Microscope (AFM). $2\mu\text{m} \times 2\mu\text{m}$ image data acquired through taping mode in AFM were handled and analysed using software; Gwydion [14] and WSxM [15,] respectively. The surface morphology of the films was also determined using Zeiss Crossbeam 540 Field Emission-Scanning Electron Microscopy (FE-SEM) operated at 2.00kV. The electrical sheet resistance was determined using a Jandel Model 3R four-point

probe whereas, electrical conductivity, carrier mobility and concentration were determined by Ecopia HMS 3000 Hall Effect Measurement System. The samples solar transmittance, $T(\lambda)$, was determined using Pekin Elmer lambda 19 UV/VIS/NIR spectrophotometer in the wavelength range from 280 nm to 2380 nm. The sample thickness, t, was estimated from the Swanepoel method [16] using the formula;

$$t = \frac{\lambda_1 \lambda_2}{2[n_1 \lambda_2 - n_2 \lambda_2]} \qquad (1)$$

The refractive indices of the sample, n_1 and n_2, were determined at the two adjacent maxima (or minima) wavelengths λ_1 and λ_2 of transmittance spectra by Kramer's – Kronig model using spectrum v5.0.1 software. Using this approach, the ITO films thickness was estimated to be 375 nm.

3   Results and discussion

3.1   XRD analysis

XRD spectra (Fig. 1) revealed that all ITO thin films showed a polycrystalline cubic structure corresponding to the Joint Committee of Powder Diffraction Standards (JCPDS) card number 71-2194 [17]. The un-exposed RTA sample maintained preferential growth in (400) plane similar to the un-annealed samples, however, this preferential growth decreased relative to (222) plane for exposed RTA samples. This decrease is related to increasing oxygen vacancies due to Sn^{+4} doping into InO_3 lattice [18] which favours (222) plane growth [19]. This reduced peak intensity suggests improved sample crystal quality as also confirmed by this sample's increased I(222)/I(400) ratio (Table 1). A similar increase in this ratio is also reported in annealed ITO films at similar temperatures in nitrogen gas [18]. Besides, this ratio decrease for un-exposed RTA sample (Table 1) suggests oxygen diffusion into this sample with this RTA exposure [8].
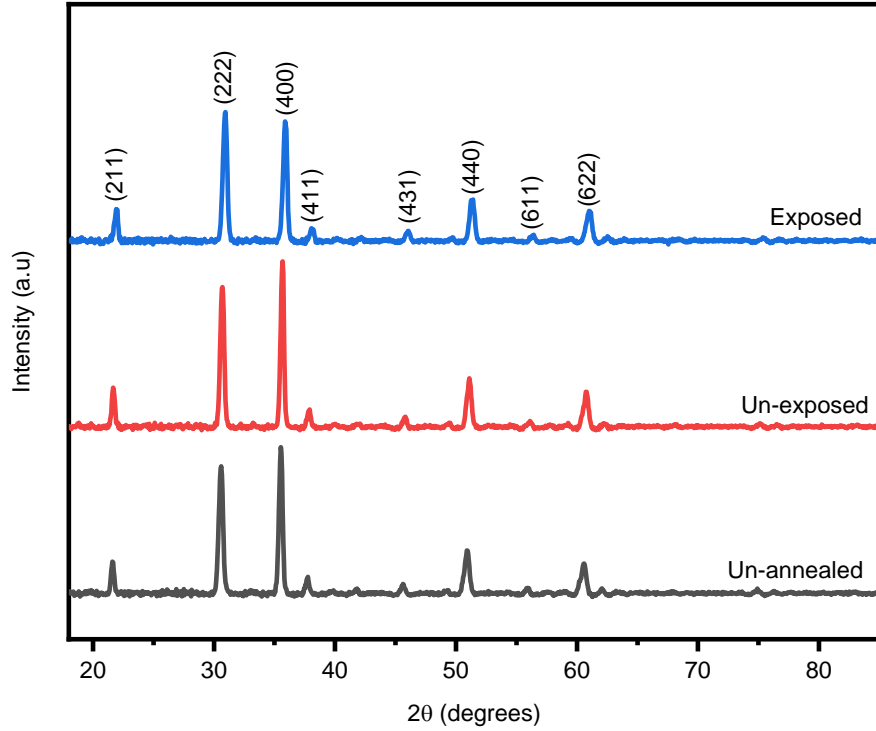
Fig. 1 XRD spectra for ITO thin films un-annealed and RTA at 550 °C for 5 minutes exposed and un-exposed to nitrogen gas

The samples' Full Width at Hall Maximum (FWHM) analysis based on (222) XRD peak, revealed slight spectra broadening for exposed and spectra narrowing for un-exposed RTA samples, as compared to the un-annealed sample (Table 1). This slight changes in FWHM suggest that RTA has the potential to preserve the crystallinity of ITO thin films [3,9]. To establish the origin of these FWHM changes, we estimated crystallite size and lattice micro-stain of these samples using a linear fit of the plot governed by the Williamson - Hall equation [20,21]

$$FWHMCos\theta = \frac{k\lambda}{D} + 4\varepsilon Sin\theta \qquad (2)$$

where θ is Bragg's diffraction angle, D is the crystallite size, λ is the wavelength of the x-ray radiation and k is the Scherer factor considered to be 0.9 for spherical crystallites. The micro-strain equals to the slope (ε) and

crystallite size (D) was determined from $FWHMCos\theta$ -intercept of the plot which is equal to $\frac{k\lambda}{D}$. This analysis

revealed that the samples' FWHM is governed by crystallite size than micro-strain (Table 1). This means, based on Scherer formula [22,23], the observed decrease in crystallite size for the exposed RTA sample implies an increase in FWHM, whereas, the observed increase in crystallite size for un-exposed RTA sample implies a decrease in FWHM. Additionally, no direct link is observed (based on the microstrain-FWHM formula [24]) between the observed FWHM trend and the samples micro-strain decrease for un-exposed and further decrease for exposed RTA samples as compared to un-annealed samples (Table 1). The decrease in crystallite size observed for exposed RTA sample (Table 1) suggests that the sample experienced a substantial nitrogen gas atmosphere, limiting the reaction [25] on the sample, and hence, reduced its crystallite size. A similar decrease in crystallite size is reported for ITO thin films annealed in nitrogen gas at lower temperatures [26,27]. Besides, crystallite size

increase for the un-exposed RTA sample as compared to the un-annealed sample (Table 1) is ascribed to further crystallization of the sample with limited nitrogen gas in this exposure. Inadequate nitrogen gas in this exposure suggests a condition which accelerates crystallization of ITO thin films [27].

The peaks position shifting to large 2θ angles for un-exposed RTA samples and further shifting for exposed RTA samples as compared to un-annealed samples (Table 1) can be explained by stress relief of RTA samples as compared to un-annealed samples and is confirmed by these samples micro-strain decrease as shown in Table 1. A similar peak position shifting is also reported for annealed ITO thin films at a similar temperature in air and nitrogen gas [18]. The stress relief is also responsible for the respective decrease in lattice constant and planar distance for these exposures (Table 1). The samples' planar distances, d, and the lattice constant, a, were computed for peaks corresponding to (222) planes based on the respective formula;

$$n\lambda = 2d \sin 2\theta \tag{3}$$

and

$$d_{hkl} = \frac{a}{\sqrt{h^2 + k^2 + l^2}} \tag{4}$$

where n is unit, λ is the X-ray wavelength 0.15406 nm, θ is the Bragg's diffraction angle in degrees, h, k, l are the Miller indices of the lattice planes.

**Table 1** FWHM, Crystallite size (D), micro-strain (ε) , crystal quality $I(222)/I(400)$, peak position (2θ) and planar distance (d) and lattice constant (a) for ITO films un-annealed, and RTA at 550 ºC for 5 minutes un-exposed and exposed to nitrogen gas

| Sample ID	FWHM (deg.)	D (nm)	$\varepsilon \times 10^{-3}$	$I(222)/I(400)$	2θ (deg.)	d (Å)	a (Å)
Un-annealed	0.40	33.7	1.58	0.88	30.5	2.92	10.12
Un-exposed	0.37	36.1	1.50	0.86	30.6	2.91	10.08
Exposed	0.41	27.8	1.21	1.06	30.9	2.89	10.01

3.2 AFM and SEM analysis

The 2D AFM images in Fig. 2 show clusters of grains for both un-annealed and RTA ITO thin films as also depicted by the FE-SEM images in Fig. 3. The images revealed that the clusters for exposed RTA sample become smaller relative to the un-annealed and un-exposed RTA samples. Further analysis of the AFM images revealed a decrease in grain size, roughness and Root Mean Square (RMS) roughness for this sample and an increase of these parameters for un-exposed RTA samples as compared to the un-annealed sample (Table 2). The grain size decrease for exposed RTA sample suggests that the sample experienced a substantial interaction with nitrogen annealing ambient, limiting the sample's reaction with residual air [25], and hence, reduced its grains size. A similar decrease in grain size and surface roughness is reported for ITO thin films annealed in a nitrogen gas [28]. On the other hand, the grain size increase with the un-exposed RTA sample is related to the crystallization of this

sample in a limited nitrogen gas atmosphere as pointed earlier in XRD analysis. A similar trend is reported for ITO thin films annealed in the air [7] suggesting limited nitrogen gas for this exposure.
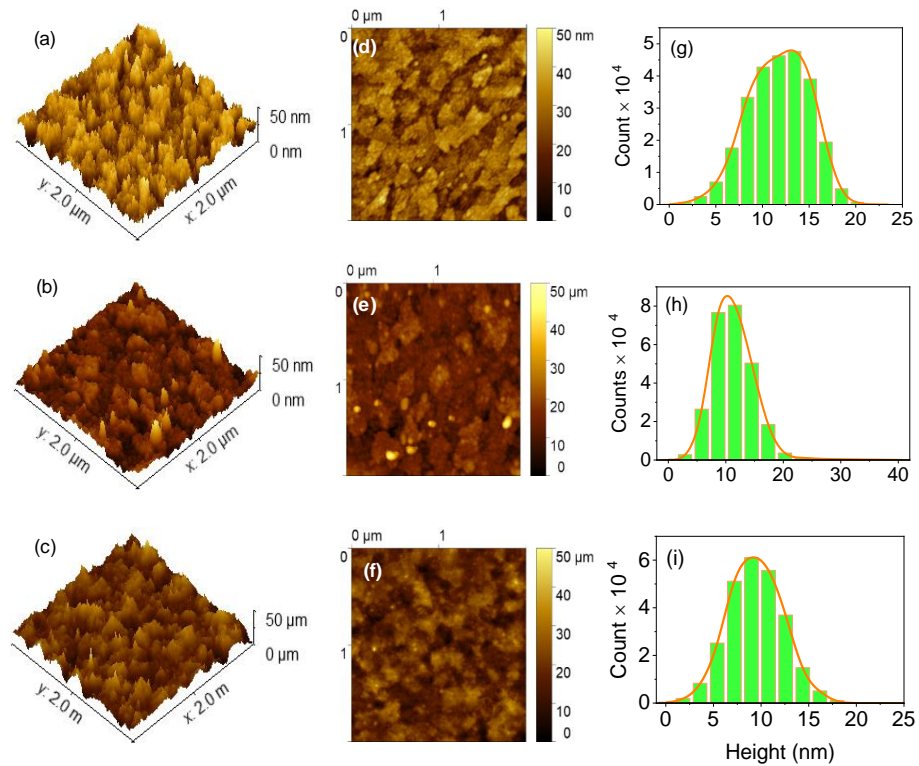
Fig. 2 2D and 3D AFM images with corresponding grain size distributions for ITO films, un-annealed (a, d, g) and RTA at 550 °C for 5 minutes un-exposed (b, e, h) and exposed (c, f, i) to nitrogen gas
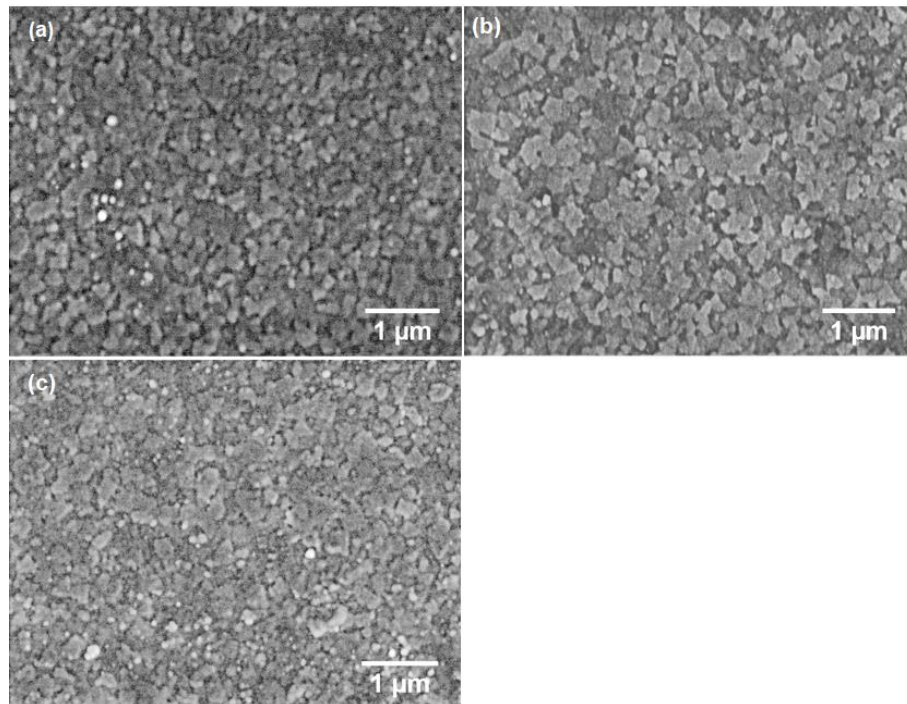
Fig. 3 FE-SEM images for ITO films un-annealed (a) and RTA at 550 °C for 5 minutes un-exposed (b) and exposed (c) to nitrogen gas

Table 2 also indicates the height asymmetry measures; skewness and kurtosis, developed from height distribution histograms of these samples shown in Fig. 2 (g-i). The skewness measures symmetry while kurtosis measures sharpness or 'peakedness' of height distribution values [29]. The skewness value was observed to change from negative for an un-annealed sample to a positive value for un-exposed and exposed RTA samples (Table 2), an indication of considerable height values below the average for un-annealed samples and considerable height values above average for un-exposed and exposed RTA samples. This implies that the surface height is determined by valleys for un-annealed samples and peaks for un-exposed and exposed samples [30]. Relative high skewness observed for un-exposed RTA sample indicates relative high peak values above the average. Besides, high kurtosis value was observed for un-exposed RTA sample relative to the un-annealed and exposed RTA sample (Table 2). This implies that RTA reduced the number of extreme heights above the surface for exposed sample (Fig. 2b), indicated by a sharper height distribution for this sample (Fig. 2h) than for un-annealed samples (Fig. 2c) with many moderated heights above the surface (Fig. 2a). On the other hands, a kurtosis value close to 3 was recorded for exposed RTA samples (Table 2) indicating a nearly normally distributed heights shape [31] as depicted in Fig. 2(i). This suggests a more uniform surface which is useful for optoelectronic applications [32].

Table 2. Surface parameters for ITO films un-annealed and RTA at 550 $^{\circ}$C for 5 minutes, exposed and unexposed to nitrogen gas

Sample identity	Grain size (nm)	Roughness (S_a) (nm)	RMS (S_q) (nm)	Skewness (S_{sk})	Kurtosis (S_{ku})
Un-annealed	12.6	2.68	3.27	- 0.21	2.67
Un-exposed	12.7	2.85	3.77	1.19	7.85
Exposed	10.3	2.33	2.91	0.10	3.10

3.3 Electrical properties

The electrical properties, summarized in Table 3, shows that the sheet resistance increases for un-exposed and decreases for exposed RTA sample relative to the un-annealed sample. This is consistent with the decrease for un-exposed and increases for exposed RTA sample Hall conductivities relative to the un-annealed sample as indicated in this table (Table 3). We ascribe sheet resistance decrease (electrical conductivity increase) for the exposed RTA sample to carrier concentrations increase due to oxygen vacancies increase related to further incorporation of Sn^{+4} into In_2O_3 lattice with excessive exposure of the sample to nitrogen gas. Further, the decrease in carrier mobility in this sample (Table 3) can be explained by increased carriers scattering from increased grain boundaries as a result of the decreased average gain size observed in this sample. Carrier mobility decrease may also result from increased Sn^{+4} impurity sites suggested in this exposure which is reported most important in determining the overall mobility of carriers [11].

On the other hand, the increase in carrier mobility for un-exposed RTA sample relative to the un-annealed sample Table 3) is attributed to reduced grain boundaries as a result of the observed grain size increase and possibly carrier scattering centres decrease related to reduced the Sn^{+4} impurities. We suggest impurities decrease in this

case because limited nitrogen annealing ambient facilitated oxygen diffusion into the sample [25,33] reducing Sn doping and hence Sn^{+4} ionized impurities. This is also expected to reduce oxygen vacancies [18] that resulted in the decrease of carrier concentrations and increased sheet resistance of the un-exposed RTA sample relative to the un-annealed sample as indicated in Table 3.

Table 3 Sheet resistance, electrical conductivity, carrier mobility and concentration for ITO films un-annealed and RTA at 550 °C for 5 minutes exposed and un-exposed to nitrogen gas

| Sample identity	Sheet resistance ($\Omega/\square$)	Electrical Conductivity ($\Omega^{-1}cm^{-1}$)	Carrier concentration ($\times 10^{21} cm^{-3}$)	Carrier Mobility ($cm^2V^{-1}s^{-1}$)
Un-annealed	8.40	3.81	1.10	21.6
Un-exposed	10.05	3.61	1.04	24.7
Exposed	7.90	4.10	1.36	16.5

3.4 Optical properties

Both samples (un-annealed and RTA), maintained nearly similar transmittance in the visible range of the solar spectrum (Fig. 4). This is not the case, however, with the samples' near-infrared (NIR) transmittance which sequentially increased for un-annealed, exposed and un-exposed RTA samples. This trend is likely related to changes observed in structure and morphology properties with the subsequent RTA exposures. To quantify these changes in transmittance spectra, we computed the average solar transmittance, Tsol, from Air Mass 1.5 solar irradiance, $G(\lambda)$ [34] using the relation;

$$T_{\text{sol}} = \frac{\int_{280}^{2380} G(\lambda)T(\lambda)d\lambda}{\int_{280}^{2380} G(\lambda)d\lambda} \tag{5}$$

The average solar transmittance for both exposed and un-exposed RTA samples increased relative to the un-annealed sample (inset in Fig. 4). Exposed RTA sample recorded slight high average solar transmittance than the un-exposed RTA sample. This finding was due to the absorption edge shift toward shorter wavelength resulting from increased carrier concentration observed for this exposure Table 3. This shift, related to the Burstein-Moss band filling effect [35,36] increased area under this spectrum which consequently leads to increasing average solar transmittance. Increased transmittance is also reported in the literature for annealed ITO thin films in the air and nitrogen gas [18].
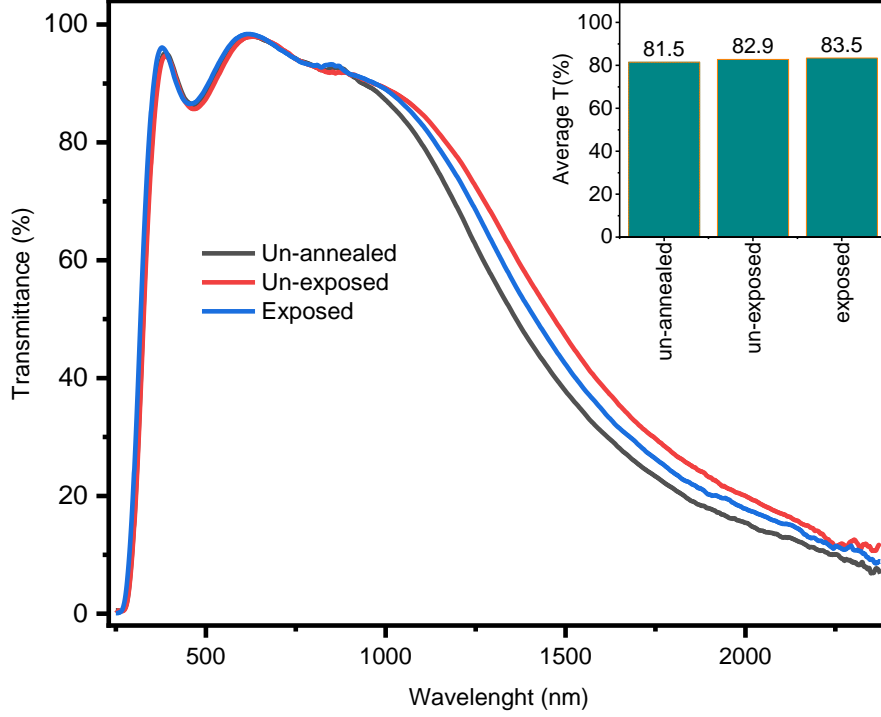
Fig. 4 Solar transmittance spectra with an inset of average solar transmittance for ITO thin films un-annealed and RTA at 550 ºC for 5 minutes exposed and un-exposed

The solar transmittance data were also used to compute the absorption coefficient (α) which was then used to estimate the' optical bandgap (E_g). This was achieved by extrapolating a linear part of $(\alpha h\nu)^2$ against photon energy $h\nu$ plot to $(\alpha h\nu)^2 = 0$. In particular, the solar transmittance (T) is related to α as [9];

$$T = A\exp(\alpha t) \tag{6}$$

whereas, for ITO thin films with a direct bandgap [7], the E_g is related to α as;

$$(\alpha h\nu)^2 = \beta(h\nu - E_g) \tag{7}$$

where A and β are constants and t is the films' thickness. Fig. 5 shows extrapolated Tauc plots for the samples from which the bandgaps were extracted. Extracted bandgaps corresponding to these extrapolations are shown in an inset of Fig. 5. These bandgaps values fall within the reported bandgap range (3.38 - 4.15 eV) for ITO thin films and within acceptable bandgap range for optoelectronic applications [7,9,18,37–39]. The bandgap related to the exposed RTA sample widens relative to the un-annealed sample. Such widening is related to Burstein-Moss band filling effects, [35,36] linked to this exposure carrier concentrations increase shown in Table 3. This means the bandgap for the exposed RTA sample widens because excess carriers in this sample block its conduction band to lowest states. In this regard, the bandgap of un-exposed RTA samples with decreased carrier concentration (Table 3) was observed to narrow.
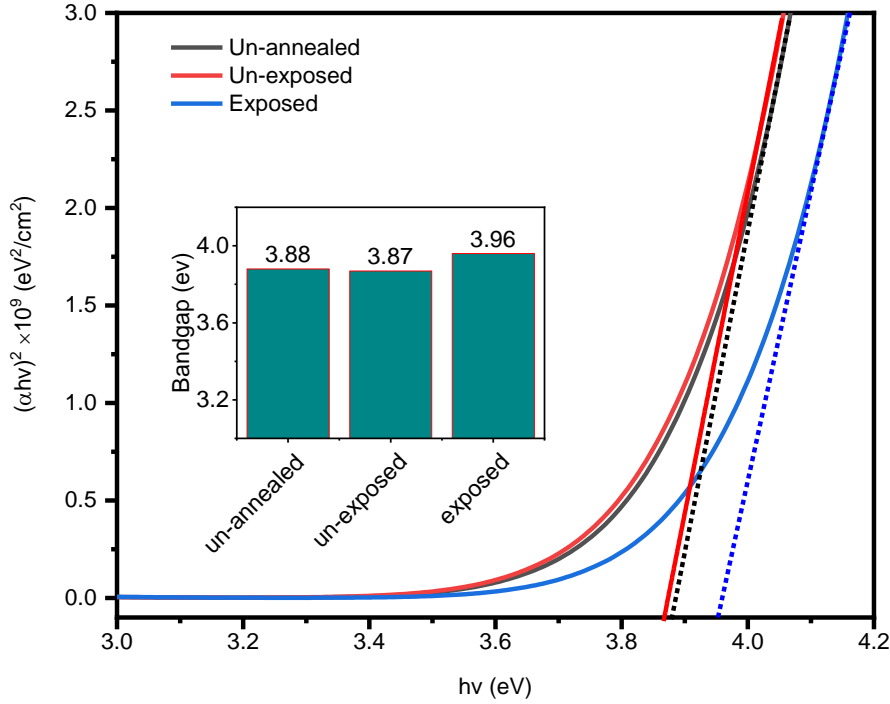
Fig. 5 $(\alpha h\nu)^2$ as a function of photon energy with an inset of the extracted bandgap for ITO thin films un-annealed and RTA at 550 °C for 5 minutes exposed and un-exposed

4 Conclusion

In this study, ITO thin films were RTA at 550 °C for 5 minutes exposed and un-exposed to nitrogen gas. The structural, morphological, optical and electrical properties of these samples were compared to the un-annealed ITO sample. The un-annealed sample showed a polycrystalline cubic structure with preferential orientation (400). This preferential orientation was maintained for un-exposed RTA sample, however, it reduces relative to (222) planes for exposed RTA sample. The crystal quality I(222)/I(400) increased for exposed RTA sample indicating improved ITO thin films quality with this exposure. Both crystallite size and grain size decreased for exposed RTA sample and increased for an un-exposed sample relative to the un-annealed sample. The surface roughness examined using AFM and FE-SEM decreased for exposed RTA sample and increased for the un-exposed sample relative to the un-annealed sample which is ascribed to the extent to which the sample was exposed to the ambient conditions during annealing. The electrical conductivity increased for exposed RTA sample and decreased for an un-exposed sample relative to the un-annealed sample. The lowest sheet resistance, highest bandgap and average solar transmittance of $7.91\,\Omega/\square$, 3.96 eV and 83 %, respectively, were observed for exposed RTA sample. Findings from this study suggest that RTA exposure have potentials to control ITO thin films properties, hence, extending its potentials applications for optoelectronics and solar cells.

Ethical standards

Conflicts of interest: The authors declare that there is no conflict of interest.

Reference

1   L. Majula, N.R. Mlyuka, M.E. Samiji, R.S. Bryce, D.Y. Kim, S.H. Kim, H.J. Lee, H.J. Choi, J. Korean Phys. Soc. (2015). https://doi.org/10.3938/jkps.67.1078.

2   Z. Song, S.C. Watthage, A.B. Phillips, M.J. Heben, J. Photonics Energy. (2016). https://doi.org/10.1117/1.jpe.6.022001.

3   H.K. Thabet, A.F. Al-Hossainy, M. Imran, Opt. Mater. (Amst). (2020). https://doi.org/10.1016/j.optmat.2020.109915.

4   A.A.I. Abd-Elmageed, S.M. Ibrahim, A. Bourezgui, A.F. Al-Hossainy, New J. Chem. (2020). https://doi.org/10.1039/d0nj01719a.

5   A.A.I. Abd-Elmageed, A.F. Al-Hossainy, E.M. Fawzy, N. Almutlaq, M.R. Eid, A. Bourezgui, S.M.S. Abdel-Hamid, N.B. Elsharkawy, M. Zwawi, M.H. Abdel-Aziz, M. Bassyouni, A.B. Slimane, M.S. Zoromba, Opt. Mater. (Amst). (2020). https://doi.org/10.1016/j.optmat.2019.109593.

6   A.F. Al-Hossainy, M.S. Zoromba, M.H. Abdel-Aziz, M. Bassyouni, A. Attar, M. Zwawi, A.A.I. Abd-Elmageed, H.A. Maddah, A. Ben Slimane, Phys. B Condens. Matter. (2019). https://doi.org/10.1016/j.physb.2019.04.030.

7   C. Guillén, J. Herrero, Vacuum. (2006). https://doi.org/10.1016/j.vacuum.2005.10.006.

8   M.K. Chong, K. Pita, S.T.H. Silalahi, Mater. Chem. Phys. (2009). https://doi.org/10.1016/j.matchemphys.2008.11.039.

9   S. Song, T. Yang, J. Liu, Y. Xin, Y. Li, S. Han, Appl. Surf. Sci. (2011). https://doi.org/10.1016/j.apsusc.2011.03.009.

10   J. Li, Z. Jiang, P. Lin, X. Chen, L. Zhong, L. Zhang, X. Wang, Mod. Phys. Lett. B. (2019). https://doi.org/10.1142/S0217984919501781.

11   C. Guillén, J. Herrero, J. Appl. Phys. (2007). https://doi.org/10.1063/1.2715539.

12   T. Nakada, Y. Hirabayashi, T. Tokado, D. Ohmori, T. Mise, Sol. Energy. (2004). https://doi.org/10.1016/j.solener.2004.08.010.

13   P.K. Sarswat, M. Snure, M.L. Free, A. Tiwari, Thin Solid Films. (2012). https://doi.org/10.1016/j.tsf.2011.07.052.

14   D. Nečas, P. Klapetek, Cent. Eur. J. Phys. (2012). https://doi.org/10.2478/s11534-011-0096-2.

15   I. Horcas, R. Fernández, J.M. Gómez-Rodríguez, J. Colchero, J. Gómez-Herrero, A.M. Baro, Rev. Sci. Instrum. (2007). https://doi.org/10.1063/1.2432410.

16   C. Calí, M. Mosca, G. Targia, Opt. Commun. (2001). https://doi.org/10.1016/S0030-4018(01)01123-3.

17   M. Thirumoorthi, J. Thomas Joseph Prakash, J. Asian Ceram. Soc. (2016). https://doi.org/10.1016/j.jascer.2016.01.001.

18   B. Parida, Y. Gil, H. Kim, J. Nanosci. Nanotechnol. (2019). https://doi.org/10.1166/jnn.2019.16242.

19   M. Gulen, G. Yildirim, S. Bal, A. Varilci, I. Belenli, M. Oz, J. Mater. Sci. Mater. Electron. (2013). https://doi.org/10.1007/s10854-012-0768-8.

20   J.N. Fru, N. Nombona, M. Diale, Phys. B Condens. Matter. (2020). https://doi.org/10.1016/j.physb.2019.411884.

21   G.K. Williamson, W.H. Hall, Acta Metall. (1953). https://doi.org/10.1016/0001-6160(53)90006-6.

22   H.B. Sawa, M.E. Samiji, N.R. Mlyuka, Tanzania J. Sci. (2018). https://doi.org/10.4314/tjs.v44i4.

23   A.F. Al-Hossainy, M.R. Eid, M.S. Zoromba, Mater. Chem. Phys. (2019). https://doi.org/10.1016/j.matchemphys.2019.04.065.

24   H. Zhao, J. Xie, A. Mao, A. Wang, Y. Chen, T. Liang, D. Ma, Materials (Basel). (2018). https://doi.org/10.3390/ma11091634.

25   Y. Hu, X. Diao, C. Wang, W. Hao, T. Wang, Vacuum. (2004). https://doi.org/10.1016/j.vacuum.2004.01.081.

26   A.S.A.C. Diniz, C.J. Kiely, I. Elfalla, R.D. Pilkington, A.E. Hill, Renew. Energy. (1994). https://doi.org/10.1016/0960-1481(94)90373-5.

27   A.S.A.C. Diniz, Renew. Energy. (2011). https://doi.org/10.1016/j.renene.2010.09.005.

28   O. Boussoum, M.S. Belkaid, C. Renard, G. Halais, F. Farhati, J. Nano- Electron. Phys. (2019). https://doi.org/10.21272/jnep.11(2).02010.

29   P. Eaton, Atomic Force Microscopy, Oxford University Press, New York, 2010.

30   O. Malik, F.J. De La Hidalga-Wade, J. Mater. Res. (2015). https://doi.org/10.1557/jmr.2015.159.

31   M. Ramzan, E. Ahmed, N.A. Niaz, A.M. Rana, A.S. Bhatti, N.R. Khalid, M.Y. Nadeem, Superlattices Microstruct. (2015). https://doi.org/10.1016/j.spmi.2015.02.030.

32   A.F. Al-hossainy, M. Sh, J. Alloys Compd. (2019). https://doi.org/10.1016/j.jallcom.2019.03.118.

33   S.K. Park, J.I. Han, W.K. Kim, M.G. Kwak, Thin Solid Films. (2001). https://doi.org/10.1016/S0040-6090(01)01489-4.

34   U.S. Department of Energy (DOE)/NREL/ALLIANCE, (1999). http://rredc.nrel.gov/solar/spectra/am1.5/ (accessed March 17, 2020).

35   E. Burstein, Phys. Rev. (1954). https://doi.org/10.1103/PhysRev.93.632.

36   A. Walsh, J.L.F. Da Silva, S.H. Wei, Phys. Rev. B - Condens. Matter Mater. Phys. (2008). https://doi.org/10.1103/PhysRevB.78.075211.

37   A.F. Al-Hossainy, M.S. Zoromba, O.A. El-Gammal, F.I. El-Dossoki, Struct. Chem. (2019). https://doi.org/10.1007/s11224-019-1289-3.

38   A.F. Al-Hossainy, M. Bassyouni, M.S. Zoromba, J. Inorg. Organomet. Polym. Mater. (2018). https://doi.org/10.1007/s10904-018-0945-1.

39   P. Prepelita, I. Stavarache, D. Craciun, F. Garoi, C. Negrila, B.G. Sbarcea, V. Craciun, Beilstein J. Nanotechnol. (2019). https://doi.org/10.3762/bjnano.10.149.